Stratified Assemblies of Magnetite Nanoparticles and Montmorillonite Prepared by the Layer-by-Layer Assembly

ARTICLE *in* LANGMUIR · MARCH 2000

Impact Factor: 4.46 · DOI: 10.1021/la990957j

4 AUTHORS, INCLUDING:

John Ostrander
University of Tulsa
12 PUBLICATIONS **1,186** CITATIONS
SEE PROFILE

Nicholas Kotov
University of Michigan
445 PUBLICATIONS **26,720** CITATIONS
SEE PROFILE

Stratified Assemblies of Magnetite Nanoparticles and Montmorillonite Prepared by the Layer-by-Layer Assembly

Arif Mamedov, John Ostrander, Farkhad Aliev,† and Nicholas A. Kotov*

Department of Chemistry, Oklahoma State University, Stillwater, Oklahoma 74078, and Departamento Fisica Materia Condensada, Universidad Autonoma de Madrid, Cantonlanco, 28049 Madrid, Spain

Received July 19, 1999. In Final Form: January 19, 2000

Hybrid thin films are prepared from 8 to 10 nm Fe_3O_4 nanoparticles and exfoliated montmorillonite clay by using layer-by-layer assembly on poly(diallyldimethylammonium bromide), PDDA. Distinct stratification of the Fe_3O_4/PDDA/clay films is obtained due to the sheetlike structure of the clay particles. This feature distinguishes these assemblies from their polyelectrolyte−polyelectrolyte analogues, where the layers of individual polyelectrolytes are strongly interdigitated. Being adsorbed on PDDA strictly parallel to the substrate surface, montmorillonite produces a dense layer of overlapping alumosilicate sheets, which virtually flawlessly separates one magnetite layer from another. The difference in magnetic properties between assemblies of various architectures is attributed to the insulation effect of clay layers inserted between magnetic layers. The montmorillonite sheets disrupt the electron exchange interactions between the magnetite nanoparticles in adjacent layers, thereby limiting the magnetization reversal to two dimensions. Some optical properties of Fe_3O_4/PDDA films are investigated as well. When they are deposited on thin plastic substrate, oscillations of optical density were observed in the red part of the UV−vis spectrum. This effect, which was never been observed for conventional, thick substrates such as glass slides, stems from the interference of the light beams passed through and reflected off of the assembled film.

Introduction

Advanced materials based on inorganic nanoparticles are currently one of the most dynamic areas of chemistry. They represent significant fundamental and commercial interest with a wide range of applications including the next generation optics, electronics, sensors, and drugs.[1,2] Synthetic methods of colloid chemistry afford manipulation of their size, surface structure, and, hence, their optical, electrical, and magnetic properties.

Between the synthesis of nanoparticles and a functional device, there is a stage of their processing that typically includes the preparation of a nanoparticle coating by one technique or another. In most cases, it is necessary to augment unique physical properties of nanoparticles with mechanical characteristics of polymers. For solid-state devices, the gap between a nanocluster dispersion and a thin film is often bridged either by spin casting[1,3] or by spraying[4] or sometimes by simple painting[5] of a polymer−nanoparticle mixture. These techniques produce coatings with thicknesses typically ranging from a few nanometers to a few micrometers and different accuracies of thickness control being the highest for spin casting. At the same time for all these methods, partial phase separation of the polymer/nanoparticle solution results in microheterogeneity.

The layer-by-layer assembly (LBL) is a new method of thin film deposition that is often used for oppositely charged polymers.[6] It can also be successfully applied to the preparation of thin films of nanoparticles.[7−19] Its

* Corresponding author. E-mail: kotov@okstate.edu.
† Universidad Autonoma de Madrid.

(1) Mattoussi, H.; Radzilowski, L. H.; Dabbousi, B. O.; Thomas, E. L.; Bawendi, M. G.; Rubner, M. F. *J. Appl. Phys*. **1998**, *83*, 7965−7974.
(2) Klein, D. L.; Roth, R.; Lim, A. K. L.; Alivisatos, A. P.; McEuen, P. L. *Nature* **1997**, *389*, 699−701; Alivisatos, A. P. *J. Phys. Chem*. **1996**, *100*, 13226; Levy, B. *J. Electroceram*. **1997**, *1*, 239−272; Jose-Yacaman, M.; Mehl, R. F. *Metall Mater. Trans. A* **1998**, *29*, 713−725; Zhdanov, V. P.; Kasemo, B. *Appl. Surf. Sci*. **1998**, *135*, 297−306; Bacsa, R. R.; Kiwi, J. *Appl. Catal. B−Environ*. **1998**, *16*, 19−29; Serpone, N.; Lawless, D.; Disdier, J.; Herrmann, J.-M. *Langmuir* **1994**, *10*, 643−652; Bruchez, M. Jr.; Moronne, M.; Gin, P.; Weiss, S.; Alivisatos, A. P. *Science* **1998**, *281*, 2013−2016; Chan, W. C. W.; Nie, S. *Science* **1998**, *281*, 2016−2018.
(3) Skandan, G. in Gonsalves, K. E., Baraton, M. I., Singh, R., Hofmann, H., Chen, J. X., Akkara, J. A., Eds. Materials Research S: Warrendale, **1998**; p 351−362; De, G. T. *J. Sol.-gel. Sci. Technol*. **1998**, *11*, 289−298; Chauhan, P.; Annapoorni, S.; Trikha, S. K. *Bull. Mater. Sci*. **1998**, *21*, 381−385.
(4) Lau, M. L.; Strock, E.; Fabel, A.; Lavernia, C. J.; Lavernia, E. J. *Nanostruct. Mater*. **1998**, *10*, 723−730; Karthikeyan, J.; Berndt, C. C.; Tikkanen, J.; Reddy, S.; Herman, H. *Mater. Sci. Eng. A−Struct. Mater*. **1997**, *238*, 275−286.
(5) Goebbert, C.; Aegerter, M. A.; Burgard, D.; Nass, R.; Schmidt, H.; in Beaucage, G., Mark, J. E., Burns, G. T., Hua, D. W., Eds. Materials Research S: Warrendale, 1998; p 293−304; O'Hara, P. C.; Gelbart, W. M. *Langmuir* **1998**, *14*, 3418−3424; Ogawa, M.; Ishikawa, H.; Kikuchi, T. *J. Mater. Chem*. **1998**, *8*, 1783−1786.
(6) Decher, G. *Science* **1997**, *277*, 1232−1237. Decher, G.; Hong, J. D. *Thin Solid Films* **1992**, *210/211*, 831. Decher, G.; Hong, J. D. *Ber. Bunsen−Ges. Phys. Chem. Chem*. **1991**, *95*, 1430. Stockton, W. B.; Rubner, M. F. *Macromolecules* **1997**, *30*, 2717−2725. Ferreira, M.; Cheung, J. H.; Rubner, M. F. *Thin Solid Films* **1994**, *244*, 806−809. Hsieh, M. C.; Farris, R. J.; McCarthy, T. J. *Macromolecules* **1997**, *30*, 8453−8458. Lvov, Y.; Onda, M.; Ariga, K.; Kunitake, T. *J. Biomater. Sci.−Polym. Ed*. **1998**, *9*, 345−355. Lvov, Y.; Decher, G.; Haas, H.; Mohwald, H.; Kalachev, A. *Physica B* **1994**, *198*, 89−91.
(7) Kotov, N. A.; Dekany, I.; Fendler, J. H. *J. Phys. Chem*. **1995**, *99*, 13065−13069.
(8) Keller, S. W.; Kim, H. N.; Mallouk, T. E. *J. Am. Chem. Soc*. **1994**, *116*, 8817−8818.
(9) Cassegneau, T.; Mallouk T. E.; Fendler, J. H. *J. Am. Chem. Soc*. **1998**, *120*, 7848−7859.
(10) Liu, Y. J.; Wang, A. B.; Claus, R. O. *Appl. Phys. Lett*. **1997**, *71*, 2265−2267.
(11) Rosidian, A.; Liu, Y. J.; Claus, R. O. *Adv. Mater*. **1998**, *10*, 1087.
(12) Kotov, N. A.; Magonov, S.; Tropsha, E. *Chem. Mater*. **1998**, *10*, 886−895.
(13) Kotov, N. A. *Nanostruct. Mater*. **1999**, *12* (5−8), 789−796.
(14) Kotov, N. A.; Haraszti, T.; Turi, L.; Zavala, G.; Geer, R. E.; Dekany, I.; Fendler, J. H. *J. Am. Chem. Soc*. **1997**, *119*, 6821−6832.
(15) Lvov, Y.; Ariga, K.; Onda, M.; Ichinose, I.; Kunitake, T. *Langmuir* **1997**, *13*, 6195−6203.
(16) Caruso, F.; Lichtenfeld, H.; Giersig, M.; Mohwald, H. *J. Am. Chem. Soc*. **1998**, *120*, 8523−8524.
(17) Kleinfeld, E. R.; Ferguson, G. S. *Science* **1994**, *265*, 370−373.

10.1021/la990957j CCC: $19.00
Published on Web 03/22/2000

simplicity and universality combined with the high quality of films with uniform distribution of nanoparticles makes the perspectives of this technique particularly strong both in research and in industry. LBL is especially suitable for the production of the films in the nanometer range with vertical organization of different sandwich-like layers. The feasibility of the use of LBL films of nanoparticles in a number of advanced electronic and photonic applications has been demonstrated.[20]

The LBL of nanoparticles can be described as the sequential adsorption of monolayers of nanoparticles on oppositely charged layers of a polyelectrolyte. Interestingly, purely inorganic LBL films were described by R. J. Iler more than thirty years ago.[21] The deposition of the films can be perfomed in a cyclic manner, which is made possible by the overcompensation of surface charge, which often takes place when polyelectrolytes and other high molecular weight species are adsorbed to a solid−liquid interface.[22] The electrostatic attraction between a semiconductor colloid and a layer of polyelectrolyte ensures the facile adsorption. At the same time, the electrostatic repulsion between similarly charged species in solution limits the thickness of the newly formed adlayer of nanoparticles. An important contribution to the thermodynamic stability of the adsorbed layer is made by nonelectrostatic interactions.[13,23] Among some advantageous features of LBL, the tolerance to the substrate's shape and material and the dual, organic−inorganic nature of the coatings should be mentioned. Unlike methods with in situ formation of nanoparticles,[24,25] the LBL technique employs premade nanoparticles, which provides much higher degree of control over their properties.

Since organic−inorganic nanostructured LBL films are still in the early stages of their development, one of the primary objectives of this study is to expand the numbers of polyelectrolyte−nanoparticle pairs to which this technique can be applied and to investigate the structure of the films. The selection of magnetic nanoparticles rather than semiconductor or metal clusters for the assembly was governed by the following factors: (1) the challenge of the preparation of functional hybrid magnetic materials; (2) the possibility of novel magnetic, magnetooptical, and magnetoresistive phenomena expected for such systems; (3) the opportunity to vary interactions between the individual nanoparticles by varying the film structure; and (4) the availability of core−shell magnetic nanoparticles, suitable for the LBL assembly of advanced materials.[19]

The preparation of the hybrid magnetic films and interlayer interactions are addressed in this publication. The LBL assembly of core−shell magnetite is a subject of our continuous work.[19,26,27] The magnetooptical and magnetoresistive properties of the LBL films of nanoparticles will be addressed in subsequent publications.

In an ideal system, the layer-by-layer nature of the process permits for the design and simple realization of sophisticated stratified structures. For polyelectrolytes, the LBL multilayers with vertical ordering approaching that of Langmuir−Blodgett multilayers have been recently reported.[28] However, for the assemblies of nanoparticles, this possibility is compromised by the high roughness of the films brought about by the aggregation of nanoparticles on polyelectrolyte chains.[26] One of the motivational factors behind the investigation of magnetite-clay multilayers is the desire to increase the complexity of LBL hybrid systems and to investigate effects associated with the layer-by-layer ordering. The roughness problem can be circumvented due to the second inorganic component used in this study, that is, natural alumosilicate montmorillonite. In aqueous dispersions, montmorillonite clay becomes exfoliated into separate sheets with an approximate diameter of 100−200 nm and a thickness of 0.9−1.0 nm. They can cover large areas, while concealing some defects of the underlying surface.[14] Being combined with layers of magnetic nanoparticles, the montmorillonite spacers can be used to vary the strength of long-range (magnetic dipoles) and short-range (exchange) interactions between the layers. Although a gradual change of magnetic properties with the number of layers has not been observed, the introduction of insulating clay layers between layers of magnetite is demonstrated to affect the process of magnetization switching and coercivity of the multilayers.

Expermental Section

Dispersions of montmorillonite and Fe_3O_4 nanoparticles were prepared as described elsewhere.[19,26] Briefly, 20 mL of 1 M $FeCl_3$ and 5 mL of $FeSO_4$ in 2 M HCl were added to 250 mL of 0.7 NH_4OH under rapid mechanical stirring for 30 min. The black solid product was decanted with the help of a magnet. The sediment was then redispersed in 50 mL of distilled water, and subsequently three aliquots of 10 mL of tetramethylammonium hydroxide solution (1 M) were added, again with rapid stirring. Finally, water was added to the dispersion up to a total volume of 250 mL. The produced particles were in the range of 8−10 nm in diameter with a size distribution of ca. 15%, as determined by transmission electron microscopy (for corresponding transmission electron microscopy images see refs 19 and 26).

Both rigid and flexible materials were used as substrates. Besides silicon wafers and glass slides, that are commonly used in LBL, a 25 μm poly(ethyleneterephthalate), PET, film (Dupont) has also been used for the sample preparation. Silicon and glass surfaces were cleaned with a hot Nochromix solution followed by thorough rinsing with deionized water. To improve the uniformity of the coating, the surface of the PET film was partially hydrolyzed by exposure to 0.1 M NaOH as depicted in ref 29. After washing with copious amount of water and drying in air, PET pieces were left in 0.5% of poly(dimethyldiallylammonium bromide), 400 000−500 000 Da (PDDA, high molecular weight,

(18) Kovtyukhova, N. I.; Ollivier, P. J.; Martin, B. R.; Mallouk, T. E.; Chizhik, S. A.; Buzaneva, E. V.; Gorchinskiy, A. D. *Chem. Mater.* **1999**, *11*, 771−778.

(19) Aliev, F. G.; Correa-Duarte, M. A.; Mamedov, A.; Ostrander, J. W.; Giersig, M.; Liz-Marzan, L. M.; Kotov, N. A. *Adv. Mater.* **1999**, *11* (12), 1006−1010.

(20) (a) Lyons, C. H.; Abbas, E. D.; Lee, J. K.; Rubner, M. F. *J. Am. Chem. Soc.* **1998**, *120*, 12100−12107. Gao, M. Y.; Richter, B.; Kirstein, S.; Mohwald, H. *J. Phys. Chem. B* **1998**, *102*, 4096−4103. Schrof, W.; Rozouvan, S.; Vankeuren, E.; Horn, D.; Schmitt, J.; Decher, G. *Adv. Mater.* **1998**, *10*, 338−341. Lenahan, K. M.; Wang, Y.-X.; Liu, Y.; Claus, R. O.; Heflin, J. R.; Marciu, D.; Figura, C. *Adv. Mater.* **1998**, *10*, 853−855. Gao, M.; Zhang, Xi.; Yang, B.; Li, F.; Shen, J. *Thin Solid Films* **1996**, *284−285*, 242−245. (b) Feldheim, D. L.; Grabar, K. C.; Natan, M. J.; Mallouk, T. E. *J. Am. Chem. Soc.* **1996**, *118*, 7640−7641.

(21) Iler, I. J. *J. Colloid Interface Sci.* **1966**, *21*, 569.

(22) Schlenoff, J. B.; Ly, H.; Li, M. *J. Am. Chem. Soc.* **1998**, *120*, 7626−7634.

(23) Shubin, V. *Langmuir* **1997**, *10*, 11093−1100. Akari, S.; Matthes, T.; Sommerhalter, C.; Boneberg, J.; Leiderer, P. *Langmuir* **1997**, *13*, 4369−4371.

(24) Schneider, T.; Haase, M.; Kornowski, A.; Naused, S.; Weller, H.; Forster, S.; Antonietti, M. *Ber. Bunsen−Ges. Phys. Chem. Chem.* **1997**, *101*, 1654−1656. Kitazawa, N. *J. Mater. Sci.* **1998**, *33*, 1441−1444. De, G. T. *J. Sol.-gel. Sci. Technol.* **1998**, *11*, 289−298.

(25) Dante, S.; Hou, Z.; Risbud, S.; Stroeve, P. *Langmuir* **1999**, *15*, 2176−2182.

(26) Correa-Duarte, M. A.; Giersig, M.; Kotov, N. A.; Liz-Marzan, L. M. *Langmuir* **1998**, *14*, 6430−6435.

(27) Pastoriza-Santos, I., Koktysh, D.; Mamedov, A. A.; Giersig, M.Kotov, N. A., Liz-Marzán, L. *Langmuir* **2000**, *16*, 2731−2735.

(28) Hong, H.; Davidov, D.; Chayet, H.; Faraggi, E. Z.; Tarabia, M.; Avny, Y.; Neumann, R.; Kirstein, S. *Supramol. Sci.* **1997**, *4*, 67−73. Tarabia, M.; Hong, H.; Davidov, D.; Kirstein, S.; Steitz, R.; Neumann, R.; Avny, Y. *J. Appl. Phys.* **1998**, *83*, 725−732.

(29) Chen, W.; McCarthy, T. J. *Macromolecules* **1997**, *30*, 78−86.

Aldrich), overnight, which was followed by rinsing and depositing of an appropriate inorganic component.

A deposition cycle consisted of the following steps: (1) adsorption of PDDA from 0.5% solution for 2 min, (2) rinsing with deionized water in three beakers for 1 min in each of them, (3) adsorption of inorganic component for 5 min, and (4) rinsing with deionized water in two beakers for 1 min in each of them. The time period for adsorption of nanoparticles was chosen on the basis of previous observations on the formation of monolayers of Fe_3O_4 reported elsewhere.[19,26] Note that the rate of adsorption may vary significantly depending on the material to be deposited. For efficient LBL, the use of adsorption times sufficient to obtain a densely packed film is suggested.

The repetition of this cycle for N times results in the deposition of N PDDA/inorganic component bilayers. LBL multilayers composed solely from magnetitie nanoparticles and polyelectrolyte are denoted here as $[M]_i$, where i is the number of repeating units, which in this case is identical to N. The composite layers combining both clay and magnetite have been assembled following several different patterns with one or more PDDA/clay, C, layers inserted between the layers of magnetite nanoparticles. Similarly to M stacks, they will be denoted here as $[CM]_i$, $[CCM]_i$, etc.

The assembly of Fe_3O_4 nanoparticles was found to be highly sensitive to the pH of the magnetite dispersion. Unlike montmorillonite, the window for a successful LBL procedure is narrow: at pH <9 the dispersion irreversibly coagulates, while the elevation of pH over 11.5 results in very low particle density due to high surface charge[13,26] and darkening of PDDA. The assembly of magnetite was carried out with freshly prepared solutions after adjusting the pH to 11.2 with a diluted solution of HCl.

Atomic force microscopy (AFM) images were taken by using a Nanoscope IIIa Multimode instrument operating in the tapping regime with TESP tips. Typically, the surface was scanned at 2 Hz with 256 lines per image resolution and a 1.2−4.0 V setpoint. No filter technique was applied to the images presented. AFM specimens on PET were attached to steel pucks with a layer of adhesive and positioned on the scanning stage of AFM, as is customary done for silicon, HOPG, or mica substrates. Virtually no effect on scanning parameters and performance of the instrument was observed when imaging films on PET as compared to the traditional AFM supports.

Magnetic measurements were performed by using a QUANTUM Design PPMS 6000 magnetometer. The magnetic field H was created by a superconducting solenoid in the persistent mode parallel to the film's surface. For the magnetic hysteresis loops, the correct demagnetization values corresponding to the sample signals were obtained by subtracting the diamagnetic signal of the substrate from the total registered signal. The linear magnetic response of PET substrates was intrapolated to the -10 kOe $< H <$ 10 kOe region from the high field wings of magnetization curves. The total magnetization signal from each specimen was scaled to the mass of the sample and UV absorption intensity at 350 nm. The saturation magnetization, M_s, of different batches of magnetite dispersions was observed to vary within a 20% interval, which was attributed to the different structure of the magnetite/solution interface affecting the average magnetic moment of nanoparticles. Multilayer systems were made from an identical magnetite dispersion within a period of a few days. Low field magnetization data have been scaled to M_s. Coercivities, H_c, were calculated as half-widths of corresponding magnetization loops at $M = 0$.

Absorption spectra in UV−vis and near-IR regions were taken with a Hewlett-Packard 8453A. Transmission electron microscopy (TEM) images were taken on a JEOL-2000 FX instrument operating at 100 kV. TEM samples were prepared so that a layer of magnetic nanoparticles was deposited only on one side of the carbon-coated TEM grid. A 200 mesh copper grid was carefully brought into contact with the surface of aqueous solutions and was allowed to float at the air−water interface for the period of time equivalent to the duration of adsorption in a regular deposition cycle. Then, the grid was cautiously removed from the solution, avoiding the contact of its backside with the subphase, and was transferred onto the surface of the next solution.

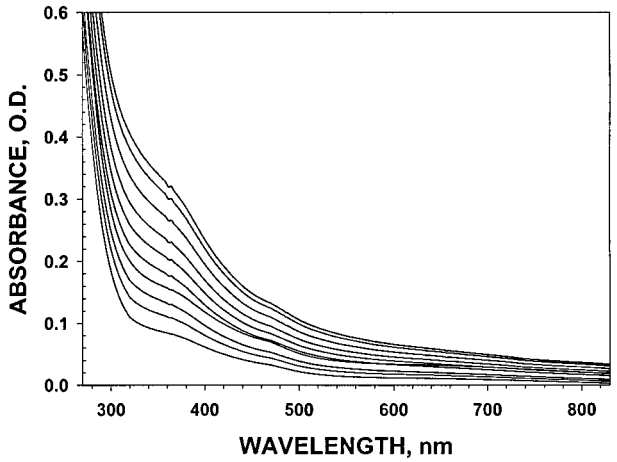

Figure 1. Absorption spectra of $[M]_i$ multilayers with $i = 1$, 2, 3, ... 10 (from bottom to top) with glass as a substrate. Small changes in the spectrum for $i = 5$ in respect to $i = 4$ and $i = 6$ in the >400 nm region are probably due to some irreproducibility in the positioning of the glass slide with respect to the light beam in the HP8453A, resulting in the superposition of refraction, scattering, and adsorption and the corresponding dispersion laws.

Results and Discussion

1. LBL Deposition of Magnetite Nanoparticles. After a suitable pretreatment procedure, which renders the surface of a solid hydrophilic, the LBL assembly of PDDA/Fe_3O_4 multilayers can be performed on a variety of substrates. The deposition on glass and other transparent substrates can be monitored as an increase of UV−vis optical density, OD (Figure 1), which in the >330 nm region originates primarily from the absorption and scattering of light by magnetic particles and their aggregates. Each deposition cycle adds a virtually constant increment to the overall film absorbency, which demonstrates that the same amount of material is transferred in each deposition cycle. The observation of OD vs N linearity must be viewed as a prerequisite for any attempt to produce vertically ordered films. Such a behavior was also observed for other inorganic species assembled by LBL such as nanoparticles,[7−10,19,20,27] and exfoliated layered compounds.[12−17,30] The growth of adsorption intensity was found to be virtually linear for 50 deposition cycles and is likely to remain so after that.[31]

2. Optical Characterization of Magnetite Films on PET. The requirements of different techniques necessitate preparation of $[M]_i$ multilayers on a variety of substrates. Besides glass, they have been assembled on silicon wafers, carbon films, and thin PET films for AFM and TEM imaging and magnetic measurements, respectively. Since PET is the least conventional substrate for the assembly of nanoparticles and, at the same time, its utilization is essential for the magnetic measurements, the structural characterization here is primarily focused on magnetite films on PET.[32] While being qualitatively similar, the UV−vis monitoring of the multilayer buildup on PET (Figure 2a) reveals unusual oscillations in the

(30) (a) Fang, M. M.; Kaschak, D. M.; Sutorik, A. C.; Mallouk, T. E. *J. Am. Chem. Soc.* **1997**, *119*, 12184−12191; Bell, C. M.; Arendt, M. F.; Gomez, L.; Schmehl, R. H.; Mallouk, T. E. *J. Am. Chem. Soc.* **1994**, *116*, 8374−8375. Lvov, Y.; Ariga, K.; Ichinose, I.; Kunitake, T. *Langmuir* **1996**, *12*, 3038−3044. (b) Kotov, N. A.; Dekany, I.; Fendler, J. H. *Adv. Mater.* **1996**, *8*, 637.

(31) Further observation of the OD vs N growth is limited by the high adsorptivity of the sample exceeding the dynamic range of spectrophotometers (OD > 4).

(32) Interestingly, PET is also employed as a base for magnetic recording tapes with a memory layer made from metal oxide particles.

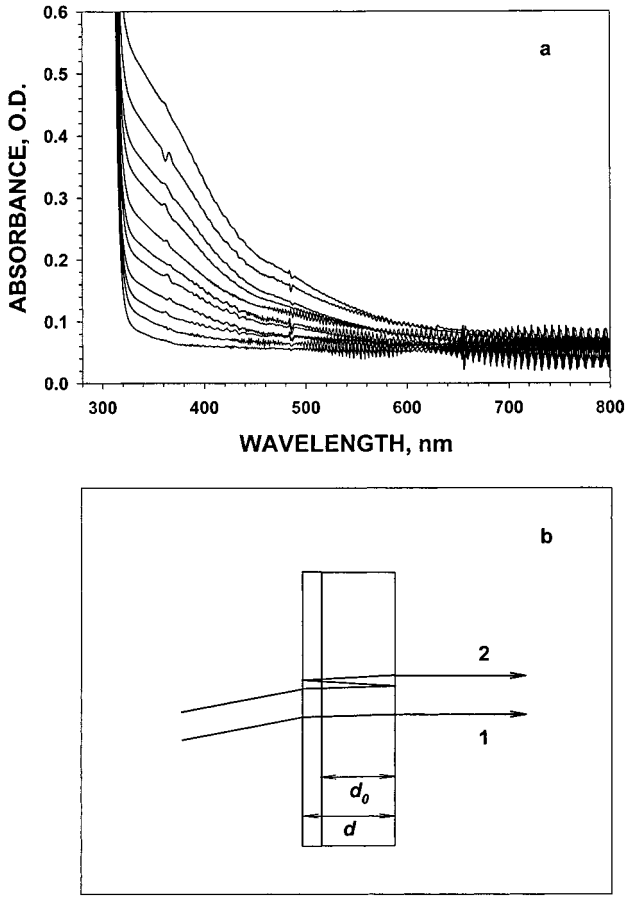

Figure 2. (a) Absorption spectra of $[M]_i$ multilayers with i = 1, 2, 3, ... 10 (from bottom to top) with hydrophilic PET as a substrate. Small changes in the spectral shape for different i in the >400 nm region are probably due to the slight irreproducibility in the positioning of the flexible PET support in respect to the light beam in the HP8453A, resulting in the superposition of refraction, scattering, and adsorption and the corresponding dispersion laws. (b) Optical scheme for the formation of diffraction ripples in absorption spectra in part a. The angle of incidence is altered for clarity.

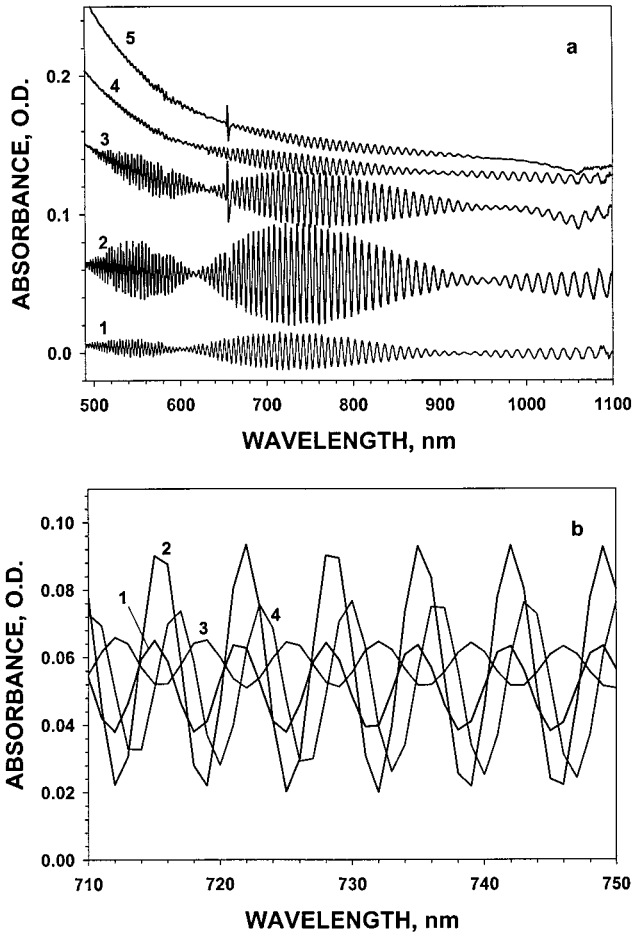

Figure 3. Details of the diffraction ripples. (a) Dependence of the amplitude of oscillations on the thickness of the $[M]_i$ magnetite overlayer for i = 0, 1, 3, 7, 10 (from bottom to top) on the PET substrate. The plots are shifted along the vertical axis for clarity. (b) Details of the diffraction ripples: the horizontal shift of the diffraction wave for a sequence of $[M]_i$ films on PET substrate; plots 1, 2, 3, and 4 correspond to i = 0, 1, 2, and 3.

near-IR part of the spectrum that have not been previously seen for LBL assemblies on glass substrates (Figure 1). These oscillations originate from the interference of transmitted beams 1 and 2 with the path and phase difference caused by the reflection from both surfaces of the thin substrate (Figure 2b). A simple expression for the period of oscillations, p, observed in the UV−vis absorption spectra can be written in terms of basic wave optics (see Appendix):

$$p(\lambda) = \lambda^2/2dn \qquad (1)$$

where λ is the average wavelength of the period in the UV−vis spectrum, d is the total thickness of the film, and n is the refractive index of the substrate. The application of this equation to the bare PET film (Figure 3a,b, curve 1) in the 715−722 nm range, taking λ = 732 nm, d = 25 000 nm, and n = 1.55,[33] yields p = 6.91 nm. The theoretical period coincides very well with an experimentally observed p = 6.8 nm (Figure 3b). For glass slides and other substrates, such oscillations cannot be seen because of substantially larger d, which means the period p must be very small (−0.2 nm for a 1 mm glass plate), and much lower intensity of the reflected beam 2.

Theoretically, the shift of the oscillation pattern allows for the calculation of the thickness of the deposited films under the assumption that the basic model of the interference does not change with the addition of $[M]_i$ coating. Within the framework of the Figure 2b model, the deposition of a 10 nm film expected for an $[M]_1$ layer should result in the red shift of the oscillations by 0.3 nm. An experimentally observed change in the oscillation pattern corresponds to a much greater shift - - as much as 4 nm for two double layers (Figure 3b, 1−3). This is indicative of an additional phase shift of the electromagnetic wave taking place at the interface between PET and the $[M]_2$ film due to the high refractive index of magnetite nanoparticles. The influence of the PET/multilayer interface can also be seen as a 3-fold increase in the amplitude of oscillations after the deposition of an $[M]_1$ layer as compared to the bare PET (Figure 3a, curves 1 and 2) associated with the increase of beam 2 intensity (Figure 2b). However, for a relatively large number of layers the amplitude of the interference ripples becomes smaller, owing to the adsorption and scattering of reflected beam 2 in the $[M]_i$ coating.

Among organic and inorganic species utilized for the preparation of the multilayers, only magnetite absorbs light in the near-UV region. The optical density at 350 nm (OD) is therefore proportional to the surface density of magnetite nanoparticles in the film. The dependence of

(33) Grigoriev, I. S.; Melikhov, E. Z. *Handbook of Physical Quantities*; CRC Press: Boca Raton, FL, 1995.

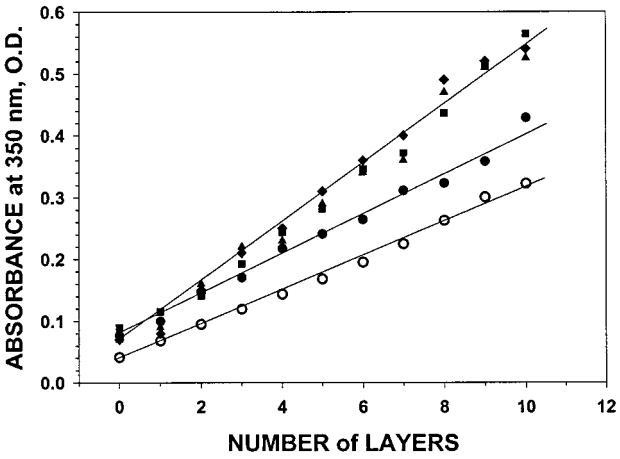

Figure 4. The dependence of optical density at 350 nm for magnetite nanoparticle multilayers of different architecture: $[M]_{10}$ on glass (○), $[M]_{10}$ on PET (●), $[CM]_{10}$ on PET (■), $[CCM]_{10}$ on PET (◆), $[CCCM]_{10}$ on PET (▲).

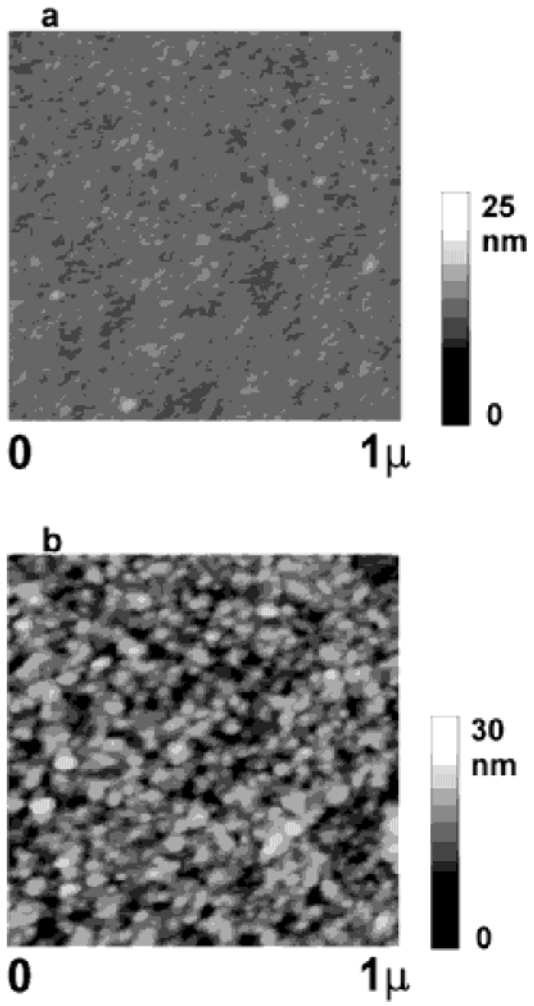

Figure 5. AFM images of PET film (a) before and (b) after surface hydrolysis. PET with the surface topography similar to the one in image b was used as a substrate for the preparation of multilayers of nanoparticles.

optical density at this wavelength on the number of layers, *N*, shows the difference in accumulation rates of magnetite nanoparticles when performing LBL on different substrates. Similarly to glass, a good linearity of the OD vs *N* plot is observed for the LBL on PET (Figure 4). The slope of the curve, $\partial(OD)/\partial N$ for PET is greater than for

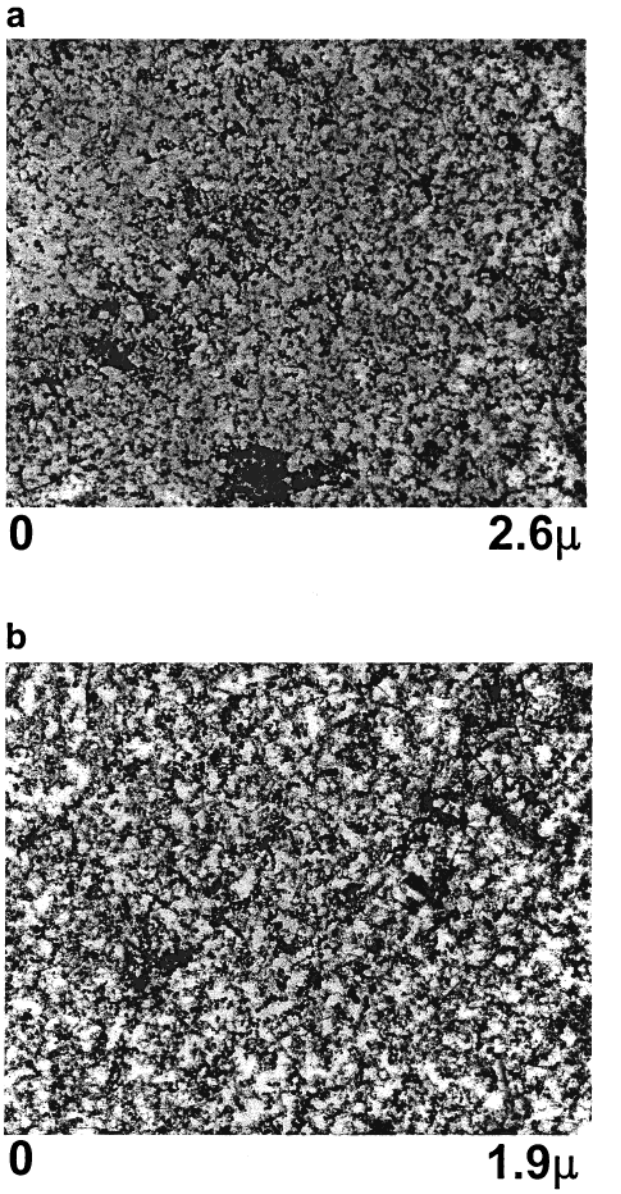

Figure 6. Transmission electron microscopy images of magnetic nanoparticles on a standard TEM copper grid bearing (a) an $[M]_1$ film and (b) a $[CM]_1$ film. Dark fields represent areas covered by nanoparticles. The average particle density on the TEM grids is expected to be lower than that on silicon wafers or PET because of hydrophobic Formvar/graphite foundation coating.

the assembly on glass, which is reflective of the difference in the quality of the underlying substrate. As can be seen from AFM scans (Figure 5), the surface hydrolysis rendering PET hydrophilic also increases the substrate roughness. This provides greater adsorption area for PDDA and subsequently for the inorganic components, which, in turn, yields the higher optical density increment.

3. Magnetite/Montmorillonite Composite Layers: Magnetic Properties. The LBL technique is applicable to a large variety of charged species and, therefore, it opens the possibility to design a structurally complex film.[7,20b,30b,34] In such assemblies, the functional properties of one inorganic material can be complemented by properties of the others. Importantly, the characteristics of the coating as a whole can be controlled by the sequence of the layers, which is determined by the dipping procedure.

(34) Lvov, Y.; Ariga, K.; Ichinose, I.; Kunitake, T. *J. Am. Chem. Soc.* **1995**, *117*, 6117−6123.

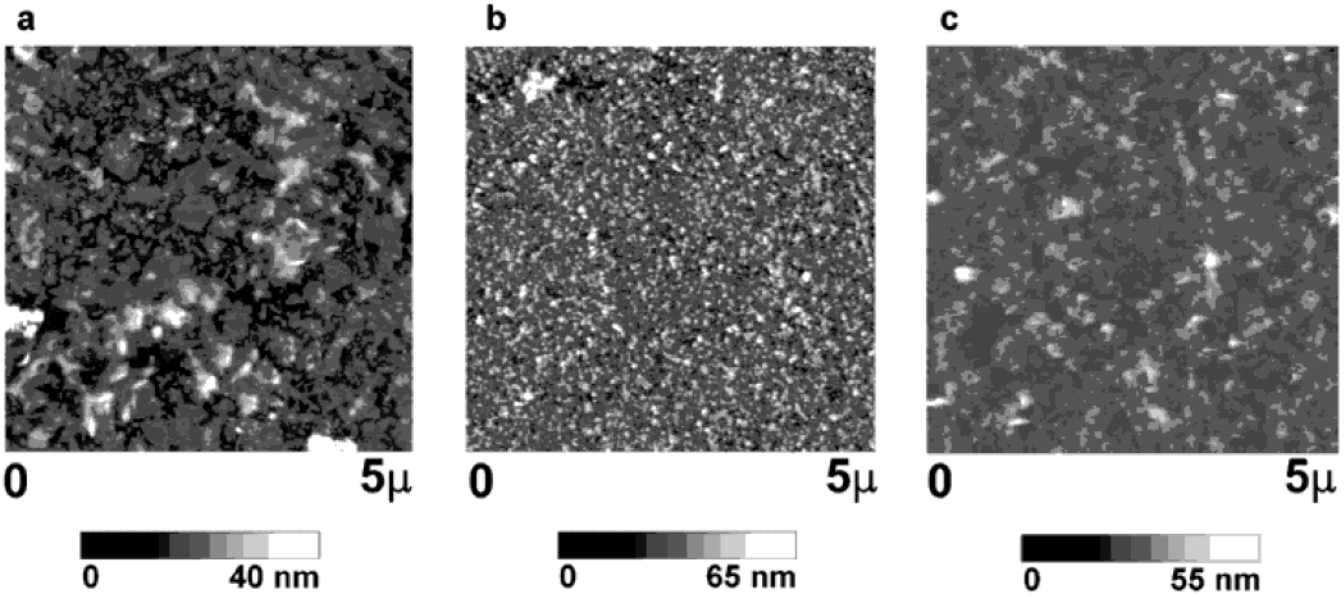

Figure 7. AFM images of (a) $[C]_1$, (b) $[CM]_1$, and (c) $[CMC]_1$ films on silicon wafers.

The possibility to vary the architecture of the LBL stack by adsorbing different inorganic components in subsequent deposition cycles can be demonstrated by interlacing the layers of magnetite with layers of montmorillonite clay C, which are known to form the LBL assemblies.[12,14,17,30a] Both of these components are negatively charged and, therefore, the preparation of M and C sandwiches can be accomplished by adsorption of the corresponding species on a layer of positively charged PDDA. Dipping the substrate with the top PDDA layer, into a dispersion of clay instead of magnetite will result in the introduction of the corresponding layer into the LBL stack. After that, the deposition procedure can be continued in the same way; the sequence of M and C layers—repetitious or not—will be determined by the dipping order.

When layers of nanoparticles are interlaced with layers of clay, the absorption-increment plots register the difference in the quality of the substrate (Figure 4). The total number of magnetite clusters deposited in each cycle increases as compared to the simple $[M]_i$ sequence. On the other hand, $\partial(OD)/\partial N$ remains virtually constant for $[CM]_i$, $[CCM]_i$, and $[CCCM]_i$ architectures. This increase in respect to $[M]_i$ should be attributed to the high negative charge of the montmorillonite surface that promotes adsorption of the positively charged polyelectrolyte. In turn, thicker PDDA "cushions" retain a greater number of Fe_3O_4 nanoparticles.

The change in particle packing in response to the variation of deposition sequence can be observed on TEM images of magnetite layers (Figure 6).[35] The increase of nanoparticle density is clearly visible when a layer of clay is introduced between the TEM grid and magnetite (Figure 6b). Additionally, the clay underlayer makes the distribution of nanoparticles more uniform. The difference in particle density can be attributed to the differences in the density of polyelectrolyte chains adsorbed in the preceding cycle. Large clay platelets bridging the gaps in the polyelectrolyte layer reduce the inhomogeneity of charge distribution, providing a more uniform surface for the second polyelectrolyte layer. A better packed polyelectrolyte layer results in more efficient adsorption of nanoparticles, which may, in fact, lead to the formation of multilayers.[36,27]

The stratified nature of the magnetite/clay assemblies can be seen on AFM scans for a $[CMC]_1$ sequence prepared on silicon wafers (Figure 7). The fine grain texture of the nanoparticle layer (Figure 7b) distinguishes it from the preceding clay layers (Figure 7a,b). When clay is deposited on top of the magnetite, the image becomes similar to that of the foundation clay layer. However, the edges of individual clay sheets cannot be seen with the same sharpness because of the high flexibility of the alumosilicate sheets[12] (Figure 7c).

The deposition of magnetic nanoparticles on PET films affords registration of magnetic properties of multilayers with little interference from the substrate. Since the mass of the deposited nanoparticles is very small, the reduction of the diamagnetic contribution from the solid support is essential for an acceptable signal-to-noise ratio of a magnetization signal from the specimens. Hence, a thin PET skin is preferred for magnetic measurements over silicon, glass, or other types of "thick" substrates. Due to the intrinsic roughness of the hydrolyzed PET, the topography features of nanoparticle and clay layers are obscured on the topography scans (Figure 8). All the images closely resemble that of PET in Figure 3b. Note, however, that the fine grain texture characteristic for nanoparticle surfaces is again more pronounced for films with the top magnetite layer (Figure 8b). A topography-independent characterization of the surface can be done by using the phase shift registration mode of the AFM instrument. The phase images are most sensitive to the strength of interactions between the tip of AFM probe and the topmost layer in the stack regardless of its relative height. As one can see, the phase scans clearly show the alternation of the surface quality when montmorillonite sheets are deposited on the layer of magnetite nanoparticles (Figure 8, right images). The high density of clay platelets forming a continuous film should also be pointed out as a feature of these assemblies. Therefore, despite

(35) For polyelectrolyte—magnetite layers deposited on carbon-coated TEM grids, the significant nonuniformity of the particles distribution may not be reflective of the film structure built on hydrophilic substrates such as glass and surface hydrolyzed PET. Carbon coating provides an unfriendly hydrophobic surface for adsorption of highly charged PDDA macromolecules, which will result in patchy adsorption.

(36) Rogatch, A.; Koktysh, D. Harrison, M.; Kotov, N. A. *Chem. Mater.* Submitted.

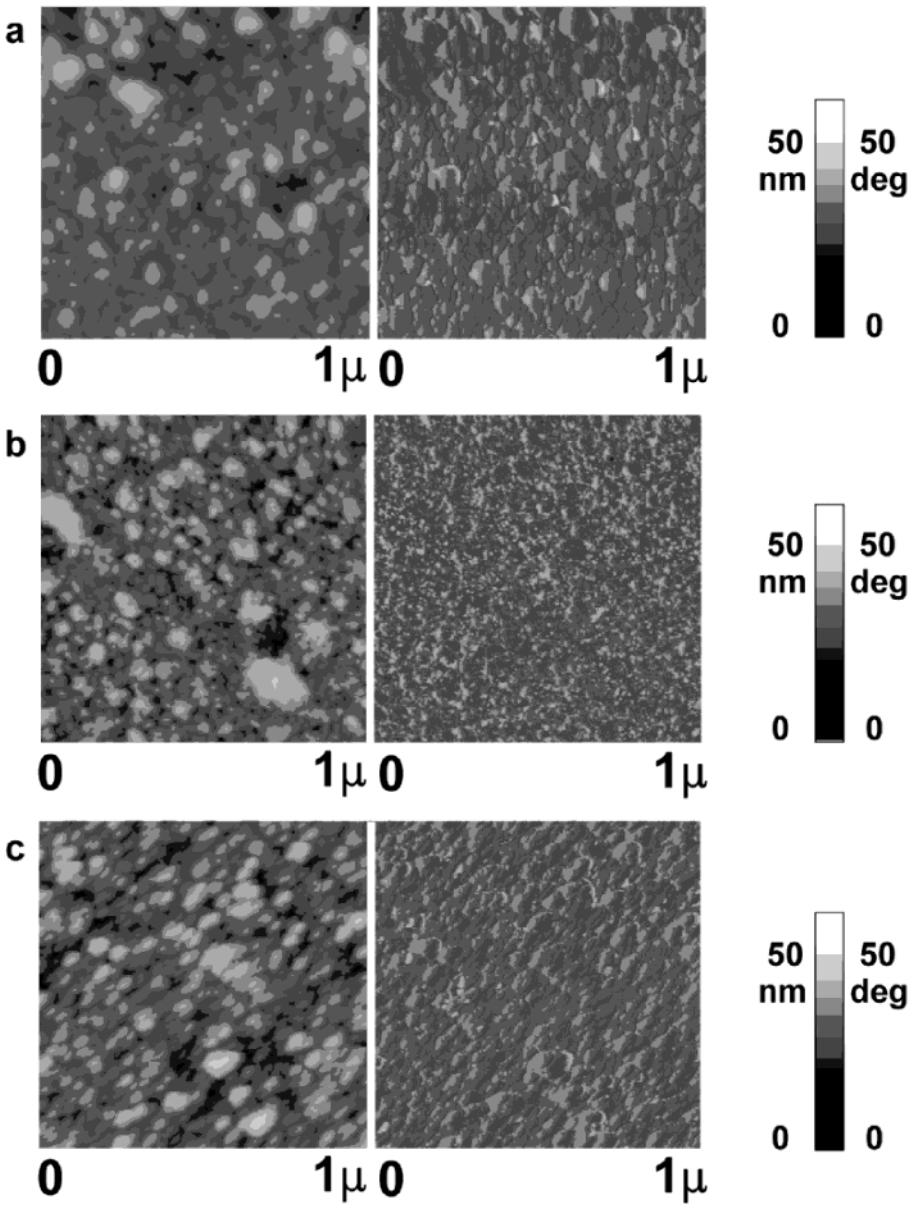

Figure 8. AFM topography (left) and phase (right) images of (a) $[C]_1$, (b) $[CM]_1$, and (c) $[CMC]_1$ films on PET.

the roughness, the magnetite layers can be completely separated from each other.

Magnetization plots of LBL films with $[M]_{10}$, $[CM]_{10}$, and $[CCM]_{10}$ architectures presented in Figure 9 display a typical superparamagnetic behavior. Normalization of the curves to the surface density of the particles and the mass of the sample renders the saturation magnetization, M_s, of a specimen independent of the structure of the multilayer, which makes the high-field plateaus for all the assemblies coincide.

The effect of the stack sequence on the magnetic behavior becomes visible for the magnetization loops taken at low-field amplitudes (Figure 10). For $T = 10$, 100, and 300 °K, all points of the two curves for $[CM]_{10}$ and $[CCM]_{10}$ fall on one another within ca. 5% deviation, whereas for $T = 10$ and 100 °K, the magnetization properties of the $(M)_{10}$ LBL assembly differs from those of $[CM]_{10}$ and $[CCM]_{10}$.

At liquid helium temperatures, the thermally activated magnetization flipping characteristic for the superparamagnetic nanoparticles becomes frustrated. The magnetization curves acquire the shape of a loop (Figure 8a)

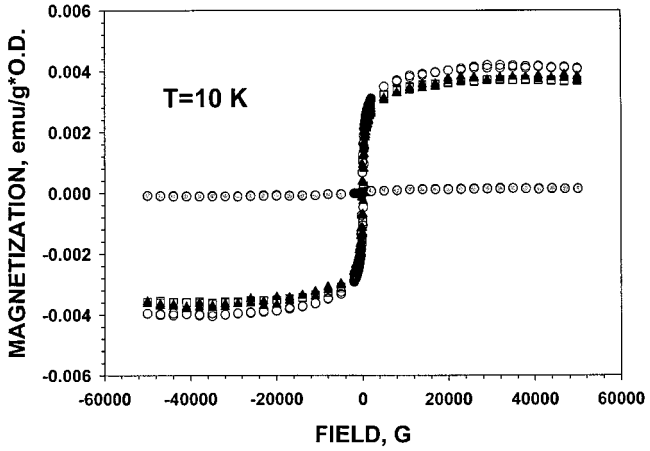

Figure 9. Normalized magnetization loops at T = 10 K for nanoparticulate films of different architecture: $[C]_{10}$ (●), $[M]_{10}$ (▲), $[CM]_{10}$ (□), and $[CCM]_{10}$ (○).

with a distinct separation of the two sweeping directions typically observed for ferromagnets. Importantly, the $[M]_{10}$ assembly displays a narrow magnetization loop with H_c

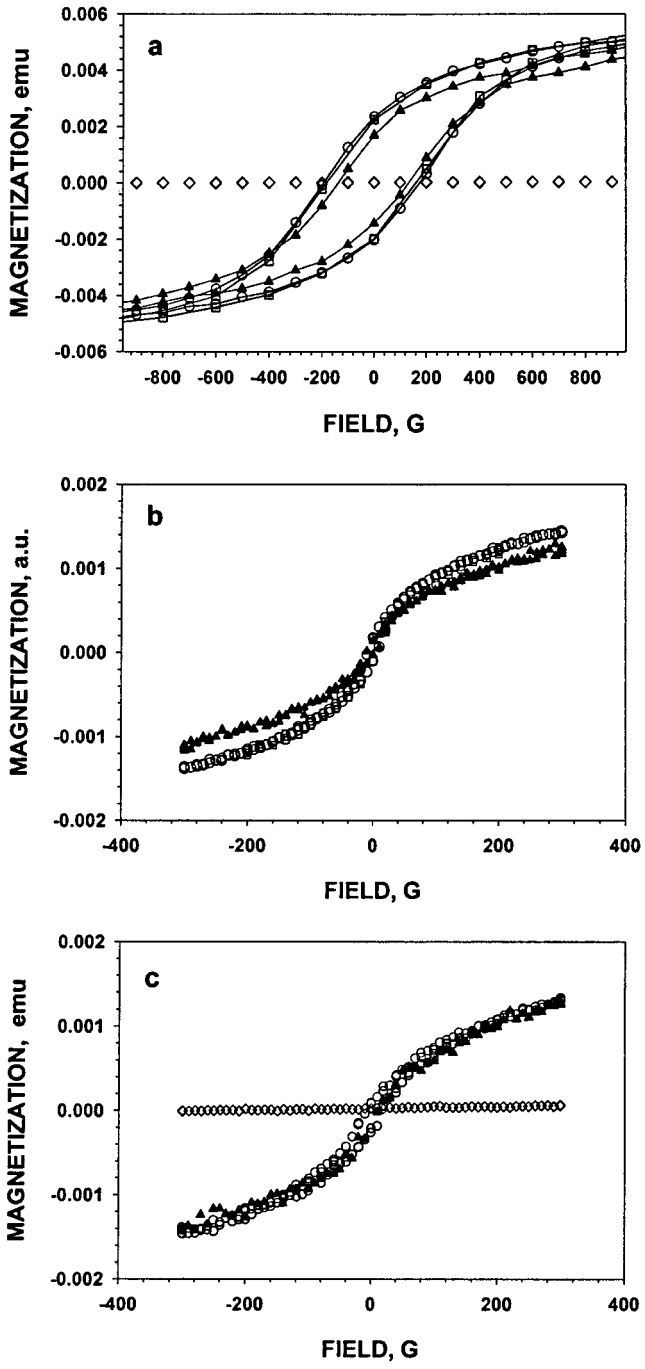

Figure 10. Low-field magnetization loops taken at (a) 10 °K, (b) 100 °K, and (c) 300 °K for nanoparticulate films of different architecture: $[C]_{10}$ (◇), $[M]_{10}$ (▲), $[CM]_{10}$ (□), and $[CCM]_{10}$ (○).

$= 140$ G, whereas $[CM]_{10}$ and $[CCM]_{10}$ assemblies display $H_c = 190$ G. For $T = 100$ °K, superpamagnetism dominates the magnetic properties of nanoparticles, nevertheless, the S-shaped magnetization curve for $[M]_{10}$ is different as compared to the coinciding ones for $[CM]_{10}$ and $[CCM]_{10}$. At $T = 300$ °C, the magnetization of $[M]_{10}$ is always the same as for the two other assemblies.

The difference in the magnetic behavior between the prepared stacks of magnetic and nonmagnetic layers can be rationalized by considering the effect of the M and C layer sequence on the magnetization switching. The reversal of the magnetization direction mostly occurs as the concerted spin flipping of adjacent magnetic domains, as represented by the Stoner−Wolfarth model.[37,38] The magnetic coupling of each nanoparticle to its neighbors is based on the short-range electron exchange and long-range magnetostatic interactions. Stronger interparticle interactions facilitate the magnetization reversal due to the falling domino effect, which macroscopically manifests in the reduction of coercivity of the material. Conversely, weaker intergrain coupling increases H_c, while reducing the squareness of the magnetization loop.[38,39]

When a layer of clay sheets is introduced between the layers of magnetite (Figure 10a), the coupling that existed between the magnetic layers is disrupted, which brings about the increase of coercivity visible at $T = 10$ °C (Figure 8a). This effect is attributed to the electrical insulation of one magnetic layer from one another, which confines spreading of the magnetization reversal to two dimensions. The thickness of the montmorillonite/PDDA bilayer is equal to 3.8−4.2 nm.[14] Typically, the range of exchange interactions is 2 nm[40] and does not exceed 4 nm in exceptional cases,[41] while the magnetostatic interaction of magnetic dipoles can span the range of a few tens of nanometeter.[42] Since no change in magnetic properties is observed between $[CM]_{10}$ and $[CCM]_{10}$ films, the effects of the multilayer structure on the magnetic properties of multilayers is attributed to the disruption of exchange interactions between adjacent layers of magnetite nanoparticles. Any further increase of the number of clay/polyelectrolyte bilayers between those of magnetite with a sequence such as $[CCCM]_{10}$ does not produce any effect on the coercivity or shape of magnetization curves—one layer of montmorillonite is sufficient to completely prevent exchange interactions between the adjacent layers.

Notably, the influence of the insulating layers on magnetic properties may appear to be small as compared to, for instance, variations of optical or electrical properties of nanoparticle assemblies caused by alteration of the film structure.[7,30b] Nevertheless, the percentage change of coercivity observed when magnetic layers of nanoparticles become isolated from each other is comparable to or greater than previously reported effects of magnetic isolation of grains stimulated by phase segregation of SiO_2, carbon, or other materials cosputtered with a magnetic metal.[43]

LBL technique makes possible the preparation of magnetic layers with large separations—on the order of 10−100 nm—that can be used to evaluate the effect of the multilayer architecture on the long-range magnetostatic interactions. However, even provided a set of specimens with proper distances, by using superparamagnetic mag-

(37) Stoner, E. C.; Wohlfarth, E. P. *Philos. Trans. R. Soc. London, Ser. A.* **1948**, *240*, 599.
(38) Himpsel, F. J.; Ortega, J. E.; Mankey, G. J.; Willis, R. F. *Adv. Phys.* **1998**, *47*, 511−597.
(39) Bottoni, G. *J. Appl. Phys.* **1991**, *69*, 4499−4501. Choe, G.; Chung, S. J.; Walser, R. M. *Thin Solid Films* **1995**, *259*, 231−236. El Hilo, M.; Chantrell, R. W.; O'Grady, K. *J. Appl. Phys.* **1998**, *84*, 5114−5122. Speliotis, D. E.; Lynch, W. *J. Appl. Phys.* **1991**, *69*, 4496−4498.
(40) Celinski, Z.; Heinrich, B. *J. Magn. Magn. Mater.* **1991**, *99*, L25-L30. Kuo, P. C.; Yao, Y. D.; Chen, J. W.; Chiu, H. C. *IEEE Trans. Magn.* **1998**, *34*, 1156−1158. Ness, H.; Gautier, F. *Phys. Rev. B.* **1995**, *52*, 7352−7361. Takahashi, Y. *Phys. Rev. B−Condensed Matter* **1997**, *56*, 8175−8182.
(41) Laget, V.; Rabu, P.; Hornick, C.; Romero, F.; Ziessel, R.; Turek, P.; Drillon, M. *Mol. Cryst. Liq. Cryst. Sci. Technol. A* **1997**, *305*, 291−301. Laget, V.; Hornick, C.; Rabu, P.; Drillon, M.; Turek, P.; Ziessel, R. N. *Adv. Mater.* **1998**, *10*, 1024. Vanlangenberg, K.; Batten, S. R.; Berry, K. J.; Hockless, D. C. R.; Moubaraki, B.; Murray, K. S. *Inorg. Chem.* **1997**, *36*, 5006−5015.
(42) Nakamura, K.; Hasegawa, H.; Oguchi, T.; Sueoka, K.; Hayakawa, K.; Mukasa, K. *Phys. Rev. B−Condensed Matter* **1997**, *56*, 3218−3221.
(43) Kaitsu, I.; Inomata, A.; Okamoto, I.; Shinohara, M. *IEEE Trans. Magn.* **1998**, *34*, 1591−1593. Liu, W. H.; Fleming, S.; Lairson, B. M. *J. Appl. Phys.* **1996**, *79*, 3651. Mukai, R.; Yamanaka, K.; Oshiki, M. *J. Appl. Phys.* **1997**, *81*, 3931−3933. Murayama, A.; Ohshima, K.; Miyamura, M.; Maekawa, M.; Kondoh, S. *J. Appl. Phys.* **1996**, *79*, 7916−7919. Murayama, A.; Hyomi, K.; Ohshima, K.; Miyamura, M.; Maekawa, M.; Kondoh, S. *J. Appl. Phys.* **1997**, *81*, 3925−3927.

netite described above, this task is difficult to accomplish because the interaction between the nanoparticles within the layer plays the dominant role in the magnetic properties. One can expect to obtain better sensitivity to interlayer separation when particles of relatively high coercivity (500−1500 G) are coated with a layer of silica, which prevents in-plane exchange coupling of nanoparticles. In that respect, the preparation of analogous films from cobalt nanoparticles can present substantial interest for the investigation of magnetic effects in layered assemblies. However, preliminary experiments in this direction revealed the problem of strong aggregation of Co nanoparticles and severe deterioration of layer-by-layer ordering, which we were able to avoid by using magnetically soft Fe_3O_4 nanoparticles. The solution of this dilemma of magnetic hardness and related aggregation is probably lying in the combination of accurately controlled particle size, surface coating, and selection of a suitable temperature range for magnetic measurements.

Conclusion

Layered assemblies of Fe_3O_4 nanoparticles can be produced on a variety of substrates by the sequential adsorption with polyelectrolyte, which yields optically uniform organic/inorganic films with a degree of vertical ordering imparted by the layer-by-layer mode of the deposition. A distinctive sandwich-like structure of the film can be obtained when introducing layers of montmorillonite clay between the layers of magnetite nanoparticles. The stacked alumosilicate sheets covering large areas of the substrate surface help to avoid interpenetration of the multilayers caused by the roughness of the layer of nanoparticles and to attain complete isolation of the magnetite layers. Stratified films from magnetite nanoparticles and montmorillonite clay with different sequences of the inorganic layers have been produced. It is demonstrated that the magnetic properties of the assemblies are affected by the multilayer architechture. For $[CM]_{10}$ and $[CCM]_{10}$ sequences, the coercivity at 10 °K increases as compared to $[M]_{10}$ films due to the disruption of electron exchange coupling between the magnetite layers.

Appendix

The condition for the constructive interference of beam 1 and 2 in Figure 2 is

$$m\lambda = 2dn \tag{2}$$

where m is an integer number. The description of other variables is given in Results and Discussion. The period of oscillations observed in Figures 2a and 3a,b is the difference between two neighboring maxima of constructive interference corresponding to m and m - 1:

$$m_1\lambda_1 = 2dn \tag{3}$$

$$(m_1 - 1)\lambda_2 = 2dn \tag{4}$$

Therefore

$$p = \lambda_2 - \lambda_1 = 2dn/(m_1 - 1) - 2dn/m_1 = 2dn/(m_1-1)m_1 \approx 2dn/m_1^2 \qquad m_1 \gg 1 \tag{5}$$

In this equation, the total number m_1 of wavelengths λ_1 fitting the path difference between the two diffracting beams is equal to

$$m_1 = 2dn/\lambda_1 \tag{6}$$

Since λ_1 and λ_2 are close to each other, instead of λ_1 in eq 6, one can use an average between λ_1 and λ_2, that is λ. Then, after the substitution of eq 6 into eq 5 one may obtain

$$p = \lambda^2/2dn \tag{7}$$

which is the equation describing the observed oscillations in the UV−vis spectrum.

The effect of the layer thickness on the position of the oscillation maximum can be described in the same way. When eq 2 is applied to two films with thicknesses of d_1 and d_2, respectively, the difference in construction interference maxima $\Delta\lambda$ corresponding to the same m can be expressed as

$$\Delta\lambda = 2d_1n/m - 2d_2n/m = 2n(d_1 - d_2)/m \tag{8}$$

A simple rearrangement of this equation gives

$$\Delta d = (d_1 - d_2) = \Delta\lambda d_0/\lambda \tag{9}$$

where d_0 is the thickness of the PET skin (25 μm, Figure 2b) with no films on it.

Acknowledgment. The authors thank reviewers for helpful comments. N.A.K. thanks NSF CAREER (CHE-9876265), AFOSR NATO (CRG 971167), OSU Sensor Center, and Nomadics Inc. for the partial financial support of this research.

LA990957J